Check for updates

View Article Online
View Journal

Energy & Environmental Science

Accepted Manuscript

This article can be cited before page numbers have been issued, to do this please use: J. Peng, M. Ou, H. Yi, X. Sun, Y. Zhang, B. Zhang, D. Yu, F. Wang, S. Gu, C. Lopez, W. Zhang, Y. Liu, J. Fang, P. Wei, Y. Li, L. Miao, J. Jiang, C. Fang, Q. Li, M. T. Fernandez-Diaz, J. A. Alonso, S. Chou and J. Han, *Energy Environ. Sci.*, 2021, DOI: 10.1039/D1EE00087J.

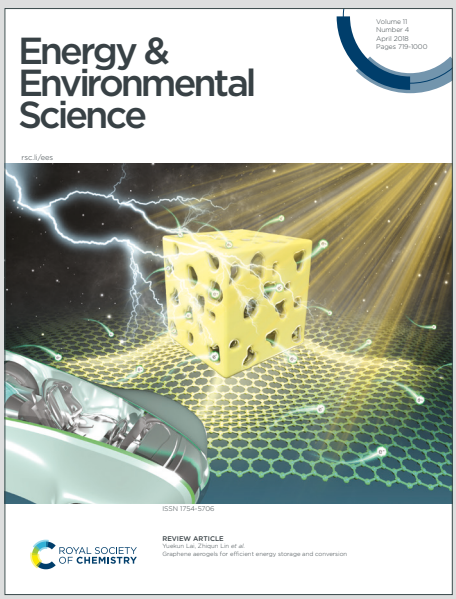

This is an Accepted Manuscript, which has been through the Royal Society of Chemistry peer review process and has been accepted for publication.

Accepted Manuscripts are published online shortly after acceptance, before technical editing, formatting and proof reading. Using this free service, authors can make their results available to the community, in citable form, before we publish the edited article. We will replace this Accepted Manuscript with the edited and formatted Advance Article as soon as it is available.

You can find more information about Accepted Manuscripts in the Information for Authors.

Please note that technical editing may introduce minor changes to the text and/or graphics, which may alter content. The journal's standard Terms & Conditions and the Ethical guidelines still apply. In no event shall the Royal Society of Chemistry be held responsible for any errors or omissions in this Accepted Manuscript or any consequences arising from the use of any information it contains.

ROYAL SOCIETY OF CHEMISTRY

rsc.li/ees

View Article Online
DOI: 10.1039/D1EE00087J

SCHOLARONE™
Manuscripts

Published on 22 March 2021. Downloaded on 3/25/2021 5:13:29 AM.

Energy & Environmental Science Accepted Manuscript

View Article Online
DOI: 10.1039/D1EE00087J

ARTICLE

Defect-free-induced Na^+ disordering in electrode materials

Jian Peng,[a,b] ‡ Mingyang Ou,[a,] ‡ Haocong Yi,[a,] ‡ Xueping Sun,[a,] ‡ Yuanpeng Zhang,[c,] ‡ Bao Zhang,[d] Yu Ding,[e] Feng Wang, [e] Songqi Gu,[f] Carlos Alberto López,[g] Wang Zhang,[a] Yi Liu,[a] Ju Fang,[h] Peng Wei,[a] Yuyu Li,[a] Ling Miao,[d] Jianjun Jiang,[d] Chun Fang,[a] Qing Li,[a] María Teresa Fernández-Díaz,[i] José Antonio Alonso,[j] Shulei Chou,[b] and Jiantao Han[a,*]

Received 00th January 20xx,
Accepted 00th January 20xx

DOI: 10.1039/x0xx00000x

For reaching a high-performance of electrode materials, it is generally believed that understanding the structure evolution and heterogeneous alignment effect is the key. Presently, a very simple and universal applicable self-healing method is investigated to prepare defect-free Prussian blue analogs (PBAs) that reach their theoretical capacity as cathode materials for sodium-ion batteries (SIBs). To direct imaging the local structure and dynamic process at the atomic scale, we deliver a fast ion-conductive nickel-based PBA that enables rapid Na+ extraction/insertion within 3 minutes and capacity retention nearly 100% over 4000 cycles. This guest-ion disordered and quasi-zero-strain nonequilibrium solid-solution reaction mechanism provides an effective guarantee for realizing long-cycle life and high-rate capability electrode materials that operate via reversible two-phase transition reaction. Unconventional materials and mechanisms that enable reversible insertion/extraction of ions in low-cost Metal-organic frameworks (MOFs) within minutes have implications for fast-charging devices, grid-scale energy storage applications, materials discovery, and tailored modification.

Broader context

Renewable energy has attracted much attention due to increasing concerns about the sustainability of fossil fuels and environmental issues. Developing sustainable and friendly ESSs is a great challenge in the 21st century. Lithium-ion batteries (LIBs) have replaced traditional energy storage devices especially in portable electronic devices and electric vehicles. However, the large-scale renewable energy requires a low-cost and high-safety energy storage systems, and the increasing demands for lithium have brought about rising cost of lithium resources. Recently, SIBs have been paid significant attention as a promising candidate for large-scale ESSs due to the abundance and low cost of sodium resources. The application of the new synthesis method has prepared new materials, and the defect chemistry of electrode materials has been deeply understood for the first time, which opens up a new route for the design of electrode materials.

Introduction

The increased consumption of fossil fuels and the intermittent nature of renewable energy resources energy requires low-cost and long-life energy storage systems for grid-connected stationary systems.[1-4] Recently, SIBs have attracted special attention in the scientific and industrial fields as alternatives to lithium-ion batteries (LIBs) because of the virtually inexhaustible and ubiquitous nature of sodium resources. The major challenge of SIBs is to find new cathode materials with a higher specific capacity and longer lifespan. Recent studies on cathode materials for SIBs have given performances comparable to their LIB counterparts.[5-8] High-performance cathode materials for SIBs should have an efficient sodium-ion insertion/extration processes because of the larger size of the Na^+ (2.04 Å) versus Li^+ ions (1.52 Å).[9-11] To date, much effort has been spent on material thermodynamic characteristics, but less on kinetic processes due to the difficulties to capture the

[a.] State Key Laboratory of Material Processing and Die & Mould Technology, School of Materials Science and Engineering, Huazhong University of Science and Technology, Wuhan 430074, P. R. China
[b.] Institute for Superconducting and Electronic Materials, Australian Institute for Innovative Materials, University of Wollongong, Innovation Campus, Squires Way, North Wollongong, NSW 2522, Australia
[c.] Neutron Science Division, Oak Ridge National Laboratory (ORNL), 1 Bethel Valley Rd, Oak Ridge, Tennessee 37831, United States
[d.] School of Optical and Electronic Information, Huazhong University of Science and Technology, Wuhan 430074, P. R. China
[e.] College of Chemistry and Materials Science, Hubei Engineering University, Xiaogan 432000, P. R. China
[f.] Shanghai Synchrotron Radiation Facility, Shanghai Institute of Applied Physics, Chinese Academy of Science, Shanghai, 201204, P. R. China
[g.] Instituto de Investigaciones en Tecnología Química (INTEQUI), UNSL, CONICET and Facultad de Quím., Bioquím. y Farm., UNSL, San Luis, 5700, Argentina.
[h.] Key Laboratory of Artificial Micro- and Nano-structures of Ministry of Education, School of Physics and Technology, Wuhan University, Wuhan 430072, China
[i.] Institut Laue Langevin, F-38042 Grenoble, France.
[j.] Department of Energy&Environment, Instituto de Ciencia de Materiales de Madrid, CSIC, Cantoblanco, E-28049 Madrid, Spain
‡These authors contributed equally to this work.
*E-mail: jthan@hust.edu.cn
Electronic Supplementary Information (ESI) available: [details of any supplementary information available should be included here]. See DOI: 10.1039/x0xx00000x

Published on 22 March 2021. Downloaded on 3/25/2021 5:13:29 AM.

Energy & Environmental Science Accepted Manuscript

View Article Online DOI: 10.1039/D1EE00087J

Published on 22 March 2021. Downloaded on 3/25/2021 5:13:29 AM.

Energy & Environmental Science Accepted Manuscript

metastable and intermediate phases during electrochemical cycling.[7, 12, 13]

More than 20,000 metal-organic frameworks (MOFs) with different constituents, sizes, geometries, and functionalities have been reported and applied in various fields such as catalysis, energy storage, and medicine.[14] MOFs are made by linking organic and inorganic units through strong bonds with a large pore aperture even up to 98 Å, which makes them become desirable candidates as host materials for rechargeable battery systems.[15-18] Prussian blue analogs (PBAs, $Na_xM_1[M_2(CN)_6]_{1-y}\square_y\bullet nH_2O$, M_1/M_2 = Fe, Co, Ni, Mn etc.; □ represents a vacancy) are a large family of low-cost transition-metal hexacyanoferrate MOFs with strong structural stability, open 3D structure, and abundant redox-active sites that have been widely studied as electrode materials for both aqueous and nonaqueous SIBs.[19-24] PBAs are typically divided into the one-electron transfer type (M_1 = Zn, Ni and M_2 = Fe, Co, Mn) and two-electron transfer type (M_1/M_2 = Mn, Fe, Co). Thus, PBAs could reach a one/two-electron redox capacity corresponding to an approximate theoretical capacity of 85 and 170 mAh g^{-1}, respectively.[25-28] Due to their high average voltage and specific capacity (≈ 450 Wh kg^{-1}), two-electron transfer type PBAs are competitive candidates to the level of $LiFePO_4$ for high energy density applications. While one-electron transfer type PBAs are desirable choices for long lifespan and fast-charging devices due to their negligible structure distortion and stability with the electrolytes.[29-31]

Goodenough and co-workers recently demonstrated that $Na_2Fe[Fe(CN)_6]$ could deliver a considerably high capacity of ~160 mAh g^{-1} with an average potential of 3.10 V[32]. Cui[25] reported that $Na_2Mn[Mn(CN)_6]$ has a highly reversible specific capacity of 209 mAh g^{-1} with an average potential of ~3.5 V corresponding to 730 Wh kg^{-1}, exceeding those of olivine $LiFePO_4$ (530 Wh kg^{-1}) and spinel $LiMn_2O_4$ (430 Wh kg^{-1}) used in commercial LIBs. These metrics make SIBs a promising alternative to LIB counterparts.[25, 33] However, most PBAs suffer from low capacity and short lifespan due to the adverse effects caused by $[Fe(CN)_6]^{3-/4-}$ vacancies and heterogeneous molecules in the lattice (e.g., coordinated water). These issues severely deteriorate the electrochemical properties of PBAs.[34-36] The adverse effects of the defects and heterogeneous molecules are threefold: 1) An increasing number of $[Fe(CN)_6]^{3-/4-}$ vacancies would bring more heterogeneous molecules and decrease active $Fe^{2+/3+}$ redox sites, resulting in fewer sites to host Na^+ and poor capacity.[32, 34, 37, 38] 2) The coordinated H_2O molecule could dissolve into the electrolyte, causing the deterioration of organic solvent and even producing safety hazards. In addition, the crystallization water may impede Na^+ transport into the lattice occupying the interstitial space of PBAs.[37, 39] 3) The crystal structure may become unstable, fragile, and even collapse during the charge/discharge process due to the randomly distributed vacancies breaking the connection of M_1-CN-M_2 bonds and forming a defective and distorted framework. Furthermore, the electronic conduction along M_1-CN-M_2 could be interrupted by the presence of $[Fe(CN)_6]^{3-/4-}$ vacancies, resulting in an increased Ohmic polarization and blockage of ions during the Na^+ insertion/desertion process.[33, 40] Thus, it is necessary to understand the heterogeneous molecular chemistry in PBAs at the atomic scale to efficiently tackle poor electrochemical properties and side reactions.

Here, using a self-healing method, we first prepared defect-free PBA frameworks with a highly ordered M_1-CN-M_2 structure. The PBAs exhibit excellent cycling and rate performance via Na^+ ion disordering with a quasi-zero-strain nonequilibrium two-phase

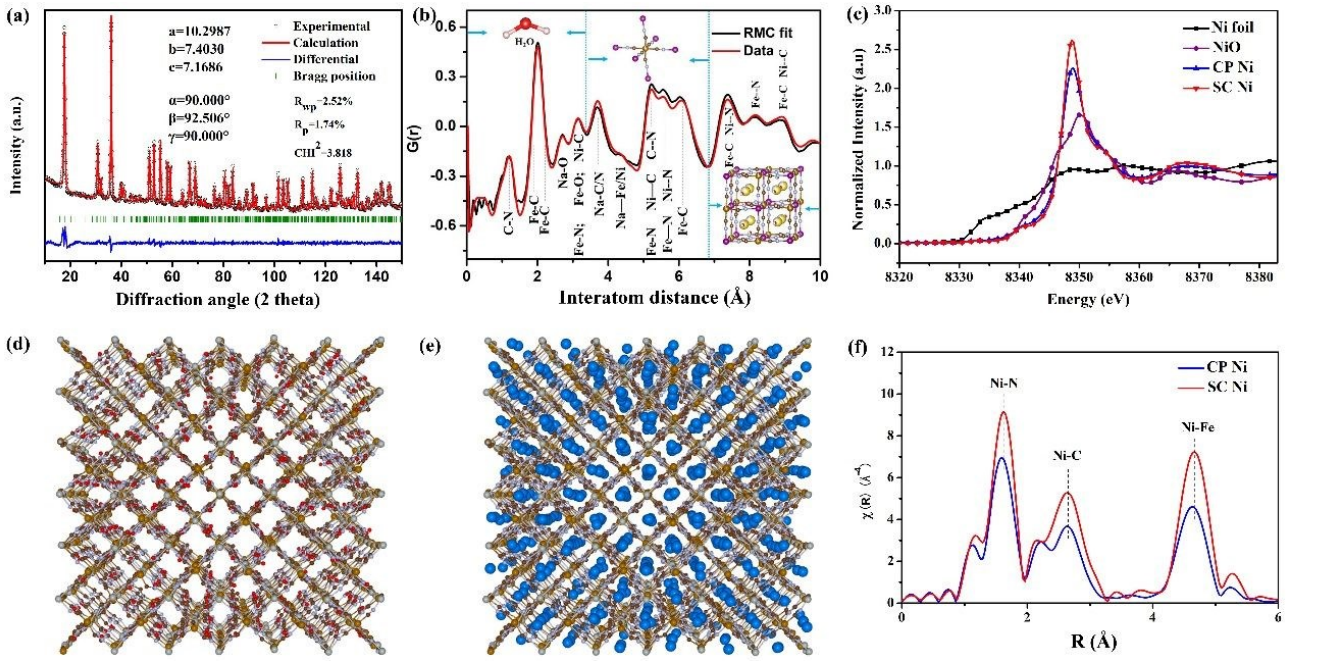

Fig. 1 | Structure analysis of SC-NiHCF. a, Neutron diffraction (ND) refinement pattern. b, Pair distribution function fitting. c, Ni K-edge XANES spectra of the as-prepared samples, and Ni foil and NiO references. d, e, Crystal structure of SC-NiHCF; FeIII is gold, NiIII is silver, O is red, and Na is blue. f, Fourier transform of EXAFS spectra at Ni K-edge with k3-weight for the as-prepared samples.

This journal is © The Royal Society of Chemistry 20xx

Please do not adjust margins

View Article Online DOI: 10.1039/D1EE00087J

Published on 22 March 2021. Downloaded on 3/25/2021 5:13:29 AM.

Energy & Environmental Science Accepted Manuscript

transition mechanism. We investigate both the origin of the quasi-solid-solution behavior and the structure-property relationships in the PBA family, especially the heterogeneous molecular characteristics using neutron powder diffraction (NPD), pair- distribution function (PDF), and extended X-ray absorption fine structure (EXAFS) techniques. We further investigate the sodiation mechanism and the effect of heterogeneous molecules based on multi-cycle *in-situ* X-ray diffraction (XRD), thermodynamic analysis, and density functional theory (DFT) calculation. A two-phase transition quasi-solid-solution sodiation mechanism and the side-effect of heterogeneous molecules are demonstrated. As a result, the single-electron-type PBAs reach their theoretical capacity alongside excellent rate performance and cycling stability of ~93.3% capacity retention over 4000 cycles at 5 C. These results lay the foundation for the development of MOF-based SIBs in the grid-scale energy storage field.

Results and discussion

Structural characterization of Ni-based Prussian blue analogs

In many materials, the crystal structure is dynamically disordered with cations free to rotate because electric fields screening of the cations are much more effective when they are free to rotate. This is consistent with our results showing that the nickel-based PBAs exhibit geometric distortion and a disorder phenomenon[41]. A stronger atomic interaction of MOF can potentially accommodate strain and stress and stabilize the configuration during the insertion and extraction of Na^+. Meanwhile, polyhedron distortion could adjust electronic tunneling among neighboring orbitals and facilitate the transfer of electrons. MOFs exhibit low electrochemical polarization as ionic and electronic conductors. The neutron diffraction patterns of the SC-NiHCF (SC stands for second crystallization) samples were refined with FullProf software to characterize their crystal structure and heterogeneous molecules[42]. Fig. 1a presents the neutron powder diffraction pattern and Rietveld refinement. The refined structure model is shown in supplementary Fig. 4. The results show that the SC-NiHCF structure is the monoclinic phase can be described within the P $2_1/n$ space group (a = 10.3043(5) Å, b = 7.4024(3) Å, c = 7.1707(3)Å, β = 92.5010(5)°).[43] The transition metal ions, Ni and Fe, are located at the 2a (0, 0, 0) and 2d (0, 0.5, 0.5) crystallographic positions, respectively. The atomic coordinates, site occupancies, and lattice parameters are shown in Table S1, and the number of non-coordinated water molecules has been estimated based on the refined number of oxygen atoms. The water molecules (or their oxygen atoms) are likely to be statistically positioned at (¼, ¼, ¼) and (¼, ¼, ¾). The results suggest a lack of H-bond interactions that would stabilize or ignore H atoms due to a lack of lone electron pairs close to the hydrogen atoms in the structure; the H_2O molecules are located close to Na atoms and form a square plane shape.

The stoichiometry refined from the NPD data agrees with the experimental values from the combination of thermo-gravimetric measurements and ICP-OES results (Table S3). The monoclinic SC-NiHCF shows higher Na^+ content, lower amount of $[Fe(CN)_6]^{3-/4-}$ defects and, crystal water molecules compared with the cubic CP-NiHCF. The local structure is illustrated in Fig. 1d and e. Owing to the superior accommodation of Na^+, the angles of ∠Ni-N-C and ∠N-C-Fe distorted from the typical 180° to 172.6° and 166.2°, respectively.

The TGA (Supplementary Fig. 3b) shows that the weight loss of SC-NiHCF is 9.8% from room temperature to 300°C, which is lower than that of the nickel-based PBAs prepared via the typical method[41, 44]. The weight loss could be assigned to the adsorbed water and interstitial water in the $[Fe(CN)_6]^{3-/4-}$ vacancies. This further suggests that SC-NiHCF has a perfect crystal structure with fewer vacancies.

Supplementary Fig. 3a shows that the diffraction peaks of (220), (420), and (440) obviously split because of the decreased symmetry and the enlarged elementary cell caused by the increased number of Na^+ per formula unit. As shown, the peaks of both HQ-NiHCF (HQ stands for high-quality) and SC-NiHCF are very strong and sharp due to the lower amount of $[Fe(CN)_6]^{3-/4-}$ defects (Supplementary Fig. 4). There are also revealed by NPD and PDF as supplementary Fig. 5 shown. Both neutron diffraction and PDF patterns of SC-NiHCF are more pronounced, indicating less $[Fe(CN)_6]^{3-/4-}$ defects in SC-NiHCF. The chemical formulas of the SC-NiHCF prepared by the new self-healing method are identified by three independent methods. Supplementary Table 2 shows the chemical formulas: i.e., $Na_{1.64}Ni[Fe(CN)_6]_{0.92}$*1.83 H_2O (by ICP-OES and TGA), and $Na_{1.48}Ni[Fe(CN)_6]_{0.97}$*1.52 H_2O (ND). These data suggest that the average amount of the $[Fe(CN)_6]^{3-/4-}$ defects are quite low, ~3% versus ~26% of the typical co-precipitation method. Even PBAs prepared by a chelating agent/surfactant-co-assisted crystallization method still have 13% defects (Supplementary Table 4).

The super-low crystal defect degree of SC-NiHCF may guarantee the effective maintenance of the crystal structure integrity during the Na^+ insertion/extraction process during the cycling.[41, 45] Here, the presence of sufficient amounts of $[Fe(CN)_6]^{3-/4-}$ ions and the high-temperature hydrothermal process could play significant roles in the kinetic process of crystal growth and self-healing. The hydrothermal reaction offers active energy to the $[Fe(CN)_6]^{3-/4-}$ ions in the solution to occupy the vacancies in the crystal lattice of PBAs and obtain well-crystallized samples with hierarchically broad nanoparticles.

Supplementary Fig. 3c shows the Fourier transform infrared (FT-IR) spectra of the three samples with typical features of PBAs. There are broad bands located at ~2090 cm^{-1} together with the Raman peaks at ~2093 and 2127 cm^{-1} attributed to the C≡N group bonding with the Ni and Fe ions. The peaks located at ~1620 and 3550 cm^{-1} are due to the H-O-H and O-H bending modes of water molecules.[37, 46] Remarkably, the defect-suppressed SC-NiHCF reveals smaller peaks at ~3500 cm^{-1} versus the defect-rich CP-NiHCF (CP stands for co-precipitation), which further confirms the above ND, and TGA results indicating fewer zeolitic and ligand water molecules occupying the crystal framework of SC-NiHCF PBAs.

Please do not adjust margins

View Article Online
DOI: 10.1039/D1EE00087J

Table 1 | Structure parameters extracted from the EXAFS fitting results of samples.

Sample	Shell	N	R (Å)	ΔE_0 (eV)	$\Delta\sigma^2$ (Å^2)	R factor (%)
CP−NiHCF	Ni-N	4.5 (±0.2)	2.03 (±0.002)	−3.0 (±0.4)	0.003 (±0.001)	0.0011
SC−NiHCF	Ni-N	5.8 (±0.1)	2.04 (±0.002)	1.0 (±0.3)	0.003 (±0.001)	0.0012

N, coordination number; R, the distance between absorber and backscatter atoms; ΔE_0 (eV), edge-energy shift (the difference between the sample and that of the theoretical model); σ^2, Debye-Waller factor (a measure of the thermal and structural disorder in absorber-scatter distances). Error bounds (accuracies) for the structural parameters obtained by EXAFS spectrum are estimated as *N* ± 20%; *R* ± 20%, σ^2± 20%, and ΔE_0 *± 20%.*

PDF pattern was fitted using RMCProfile based on reverse Monte Carlo (RMC) algorithm. Fig. 1b shows the PDF pattern (with RMC fit also presented in supplementary Fig 6-8): The first peak lies at ~1.1 Å and corresponds to C-N bonding. The second peak at 2 Å corresponds to Fe-C and Ni-N bonding. The third peak at 2.7 Å is O-related bonding (O-C, O-N, O-Na), and the fourth peak at about 3.15 Å is mainly due to Fe-N and Ni-C bonding. The fifth peak at 3.7 Å is related to Fe-O, Ni-O, C-N, N-Na, and C-Na bonding (Supplementary Fig. 11). The protuberance at about 4.32 Å implies a broad peak corresponding to Na-Ni and Na-Fe bonding. This suggests a huge displacement value for Na^+, which further has been confirmed by Reitveld-like small box fitting using PDFgui program. Supplementary Fig.10 and supplementary Fig.11 show refined patterns in different range of real space. However, the goodness of fit varies as the fitting range changes as supplementary Fig.11 shows, implies local structure exists. Thus, "big box" modeling is performed to investigate the local structural features of NiHCF. Supplementary Fig. 6 shows refined patterns based on different starting configuration and supplementary Fig. 7 displays the derived partial PDFs, all of which prove the goodness of fitting. To further investigate the structural feature of Na ions, bond angle analysis and displacement analysis are performed. Generally, Na ions were assumed to be distributed over specific crystallographic 4(e) sites with a harmonic thermal vibration around the equilibrium positions and with Na-Na-Na bond angle equal to 94.4°. However, our in-depth analysis based on RMC simulation indicates the asymmetric bond angle displacement around 87. 57°, as shown in supplementary Fig. 8. Besides, the Kernel density plots of Na displacement in Supplementary Fig. 9 shows the irregular shape, implying the huge asymmetric anharmonic thermal vibration around 4(e) sites. Further, the Kernel density plot of Na displacement in X-Z plane displays two discrete area (Supplementary Fig. 9 b), implying two individual sites of Na in X-Z plane and proving frustrated feature in NiHCF. Such effect suggests Na density is not localized at 4(e) sites but looks like a "disordered lattice liquid".[47]

To evaluate the change of local electronic and geometric structures of the metal elements in the samples, X-ray absorption fine spectroscopy (XAFS), including X-ray absorption near-edge spectra (XANES) and extended X-ray absorption fine structure (EXAFS), was performed both at the Ni K-edge and Fe K-edge (Supplementary Fig. 12). The XANES profiles at the Ni K-edge for CP-NiHCF and SC-NiHCF samples are shown in Fig. 1c along with Ni foil and NiO references. The absorption energies and the white-line peak profiles in prepared samples are quite different from the features of Ni^{2+} in the NiO reference due to the significantly different local environments. Furthermore, there is a significant decrease in the white-line intensity for the CP-NiHCF versus the SC-NiHCF. Its absorption energy also slightly shifts to lower energy, indicating a weak metal-ligand effect between Ni atoms and the neighbor ligands. Also, the intensities of the EXAFS oscillations in CP-NiHCF (Fig. 1f) are lower than that of SC-NiHCF, which demonstrates lower crystallinity or the non-saturated coordination nature in CP-NiHCF.

The corresponding Fourier transform EXAFS (FT-EXAFS) spectra at Ni K-edge without phase correction is shown in Fig. 1f. The peaks located at 1.8, 2.8, and 4.6 Å can be assigned to Ni-N, Ni-C, and Ni-Fe contributions, respectively. The intensities of the main peaks in CP-NiHCF are lower than that of SC-NiHCF. Ignoring the thermal effects, these changes can be caused by the structural changes in the Debye-Waller effect or the non-saturated coordination numbers. The EXAFS fitting parameters are listed in Table 1 via quantitative structural analysis for all samples. The coordination number of Ni-N bond in CP-NiHCF (4.5) is lower than that of SC-NiHCF (6.0) despite being by a subtle higher Debye-Waller factor. Therefore, both the XANES and EXAFS features for prepared samples demonstrate the defective nature of CP-NiHCF. This is consistent with the above analysis results.

The 3D stacking morphologies with a narrow particle size distribution of ~700 nm for SC-NiHCF are observed by scanning electron microscopy (SEM) and are shown in Supplementary Fig. 15. Close examination revealed that each secondary particle assembly comprised many regular cubic nanoparticles oriented with different angles. Owing to the different surface energies and random arrangement of the vacancies, the precursor grows into a hierarchical structure with secondary particles with rich boundaries. This can provide abundant electrode-electrolyte interfaces for the migration of Na^+ ions to further realize rapid ionic transfer and enhanced volume energy densities.[48, 49] The HR-TEM and elemental mapping (Supplementary Fig. 16) verify that the N, Fe, Ni, Na and are uniformly distributed in the sample further suggesting crystal integrity and high purity.[50, 51]

Half-cell performance

As the cyclic voltammetry (CV) curve shown in Supplementary Fig. 17, SC-NiHCF displays a pair of well-defined and symmetric oxidation/redox peaks upon reversible insertion/extraction of

Published on 22 March 2021. Downloaded on 3/25/2021 5:13:29 AM.

Energy & Environmental Science Accepted Manuscript

This journal is © The Royal Society of Chemistry 20xx

Please do not adjust margins

View Article Online
DOI: 10.1039/D1EE00087J

Published on 22 March 2021. Downloaded on 3/25/2021 5:13:29 AM.

Energy & Environmental Science Accepted Manuscript

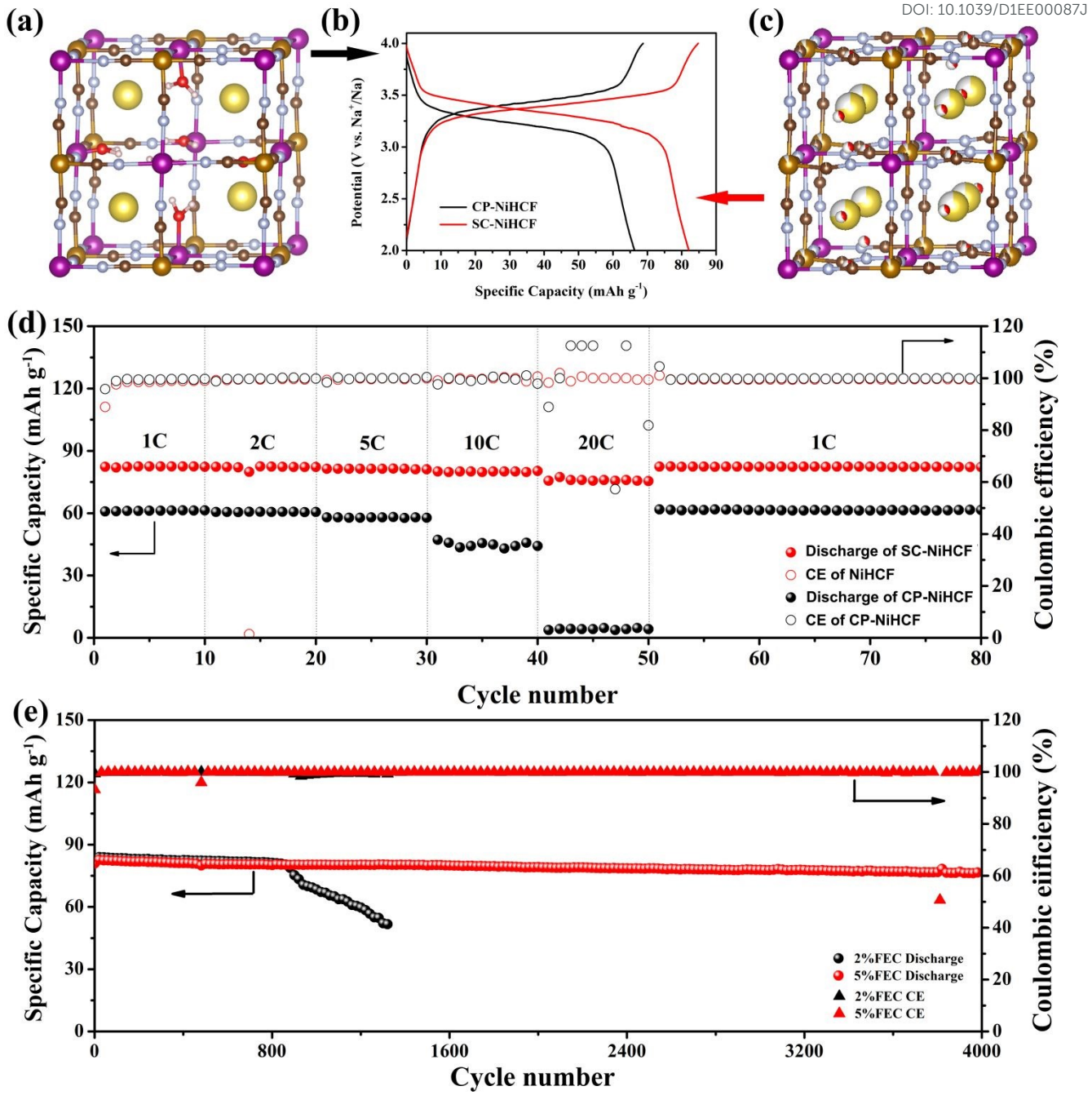

Fig. 2 | Electrochemical analysis of CP-NiHCF and SC-NiHCF electrode. a, Ball stick pattern of CP-NiHCF. **b,** Charge/discharge voltage profiles of CP-NiHCF and SC-NiHCF at a current density of 0.1 C (1 C = 80 mA g^{-1}). **c,** Ball stick pattern of SC-NiHCF. **d,** Rate capability of CP-NiHCF and SC-NiHCF from 1 to 20 C. **e,** Long-term cycling performance of SC-NiHCF in different electrolytes.

Na^+ inside the structural framework, which is attributed to the redox reaction of Fe^{2+}/Fe^{3+}. In contrast, the Ni ion is electrochemically inert within the voltage window corresponding to the typical $Na_2Ni[Fe(CN)_6]$.[52]

The electrode performances of SC-NiHCF and CP-NiHCF in sodium cells are compared in Fig. 2b and d. From 2.0 to 4.0 V, CP-NiHCF delivers 67 mAh g^{-1} of initial capacity at the rate of 8.5 mA g^{-1}. In comparison to the CP-NiHCF and HQ-NiHCF, the SC-NiHCF has a better electrode performance due to the lower content of zeolite water and fewer $[Fe(CN)_6]^{4-}$ vacancies[53]. Fig. 2a and Fig. 2c show typical structure model of CP-NiHCF and SC-NiHCF respectively where $[Fe(CN)_6]^{4-}$ is lost and replaced by H_2O in CP-NiHCF as shown at Fig. 2a. The reversible discharge capacity of SC-NiHCF reaches ~83 mAh g^{-1}, which corresponds to approximately 97.6% of the theoretical capacity based on a single-electron redox process of Fe^{2+}/Fe^{3+} couple. Moreover, SC-NiHCF can give a very high-capacity retention of 90% at the current density of 20 C.

The electrode performance is greatly influenced by adding the FEC (fluoro-ethylene carbonate) content into the electrolyte

Please do not adjust margins

View Article Online
DOI: 10.1039/D1EE00087J

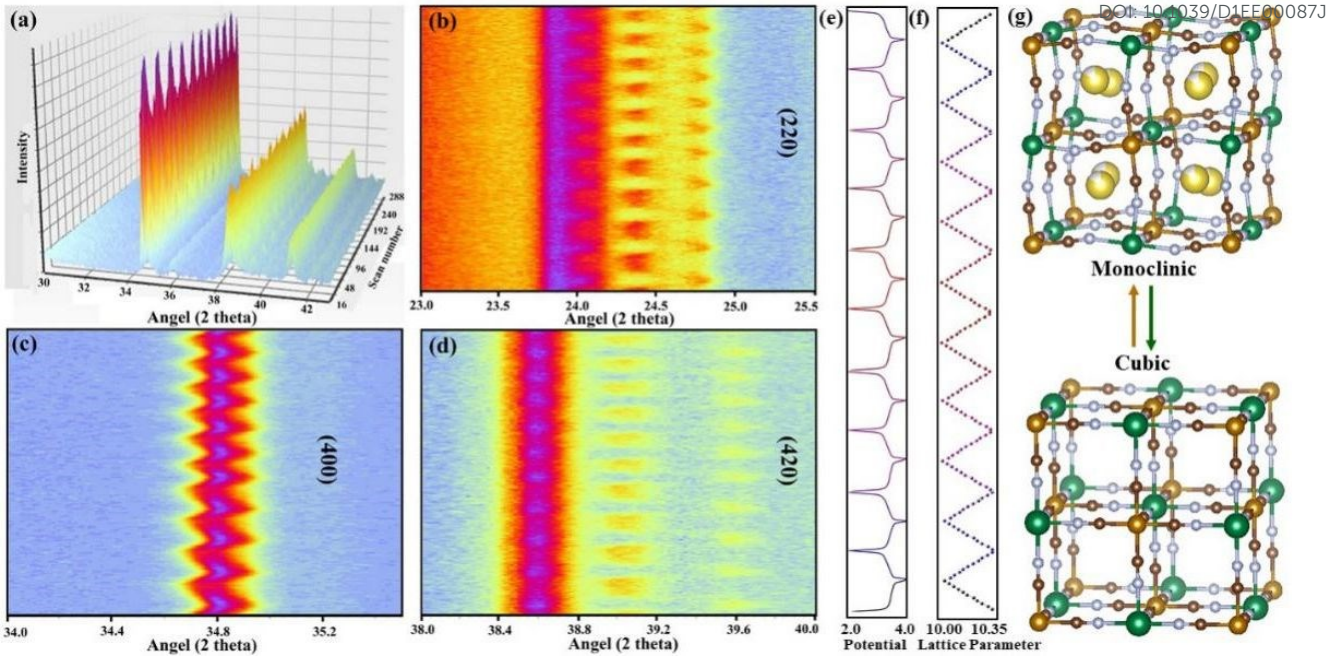

Fig. 3 | *In situ* XRD analysis of SC-NiHCF under cycling at current densities of 40 mA g^{-1}. a, Contour maps of *in situ* XRD during the first 10 cycles. **b–d,** Image plots of the (220), (400), and (420) reflections during the first 10 cycles. **e,** Galvanostatic charge/discharge curves at the current density of 40 mA g^{-1}. **f,** The corresponding charges of the lattice parameter. **g,** Structural evolution of SC-NiHCF during the charge/discharge process.

(Fig. 2e and supplementary Fig. 18-22). Both half-cells using electrolyte with 2% and 5% FEC deliver superior cyclic stability (97% of initial capacity after 850 cycles and 93.3% after 4000 cycles, respectively). This suggests that the presence of FEC in the electrolyte could improve the electrochemical performance of the cells due to the formation of denser SEI films promoted by the FEC.[48] The dual electrons transfer type cobalt-based PBAs synthesis through this self-healing method also achieved their theoretical specific capacity as shown in supplementary Fig. 23-24 which proves that this method is universally appliable. Further electrochemical performance enhancement might be achieved through optimizing the salts, solutions[54] and additives[55] of the electrolytes for practical market applications.

Sodium-ion storage mechanism

The sodium storage mechanism of SC-NiHCF was studied across multiple cycles via *in-situ* X-ray diffraction (XRD) tests with a Cu Kα X-ray source as shown in Fig. 3 and supplementary Fig. 26-27. This experiment probes the structural evolution during Na^+ insertion and extraction. Fig. 3a shows that the peak and intensity shifts retain cyclic variation indicating the quasi-solid solution reaction mechanism[6]. Remarkably, the peaks at (200), (400), and (420) show a shift in the patterns that are negligible and mainly attributed to the "quasi-zero-strain" characteristics of Ni-based PBAs and the slightly reversible shift of the lattice parameters of SC-NiHCF from 10.315 to 10.039 Å. The negligible lattice distortion is advantageous because large-scale volume variation and stress-strain leads to the collapse of the crystal framework during cycling, resulting in the irreversible capacity fading.

The (200), (220), (400), and (420) peaks slightly shift to high diffraction angles during the charging processes, which is a result of the Na^+ extraction from the crystal framework of SC-NiHCF, and the intensity of these peaks increases markedly. Interestingly, the (200) and (220) doublets converge into a single peak located at ~24°, which is related to the phase transition from monoclinic to cubic symmetry along with of the lattice parameter decreased from 10.315 to 10.039 Å.[49, 56] During the discharge process, the four peaks gradually shift to low diffraction angles, i.e., to their initial position, and the single (200) splits into the (200) and (220) peaks corresponding to the phase transition from cubic to monoclinic. Remarkably, the reversible phase transitions and high reversibility of the Na^+-ion migration are equal over the following 10 cycles.

DFT calculations were applied to understand the inner mechanism of Na^+ storage and migration in the PBA framework. Fig. 4a indicates 3 possible Na^+ interstices denoted as 8*c*, 24*d*, and 32*f* with Wyckoff notations in the space group *Fm-3m* for the cubic unit cell can host Na^+.[57] In the 3-site types, 8*c* provides the largest free space, and 24*d* offers the smallest. Furthermore, the sodiation potential of the Na adatom in both perfect and defect-rich Ni-Fe PBA frameworks is calculated by DFT. The sodiation potential (*V*s) of the Na adatom in the framework is calculated as follows:

$$Vs = -(E_{Na-PBA} - E_{PBA} - E_{Na}), \quad (1)$$

where E_{Na-PBA}, E_{PBA}, and E_{Na} are the total energies of one Na adatom adsorbed in the framework, the free framework, and the Na bulk, respectively. In the perfect Ni-Fe PBA framework, the most stable site (the highest sodiation potential) for Na adsorption is the 24*d* with a voltage of about 3.28 V. All calculated sodiation potentials in the perfect framework are above 2.5 V. However, the sodiation potential decreases dramatically with an increasing number of defects in the

Published on 22 March 2021. Downloaded on 3/25/2021 5:13:29 AM.

Energy & Environmental Science Accepted Manuscript

This journal is © The Royal Society of Chemistry 20xx

Please do not adjust margins

View Article Online
DOI: 10.1039/D1EE00087J

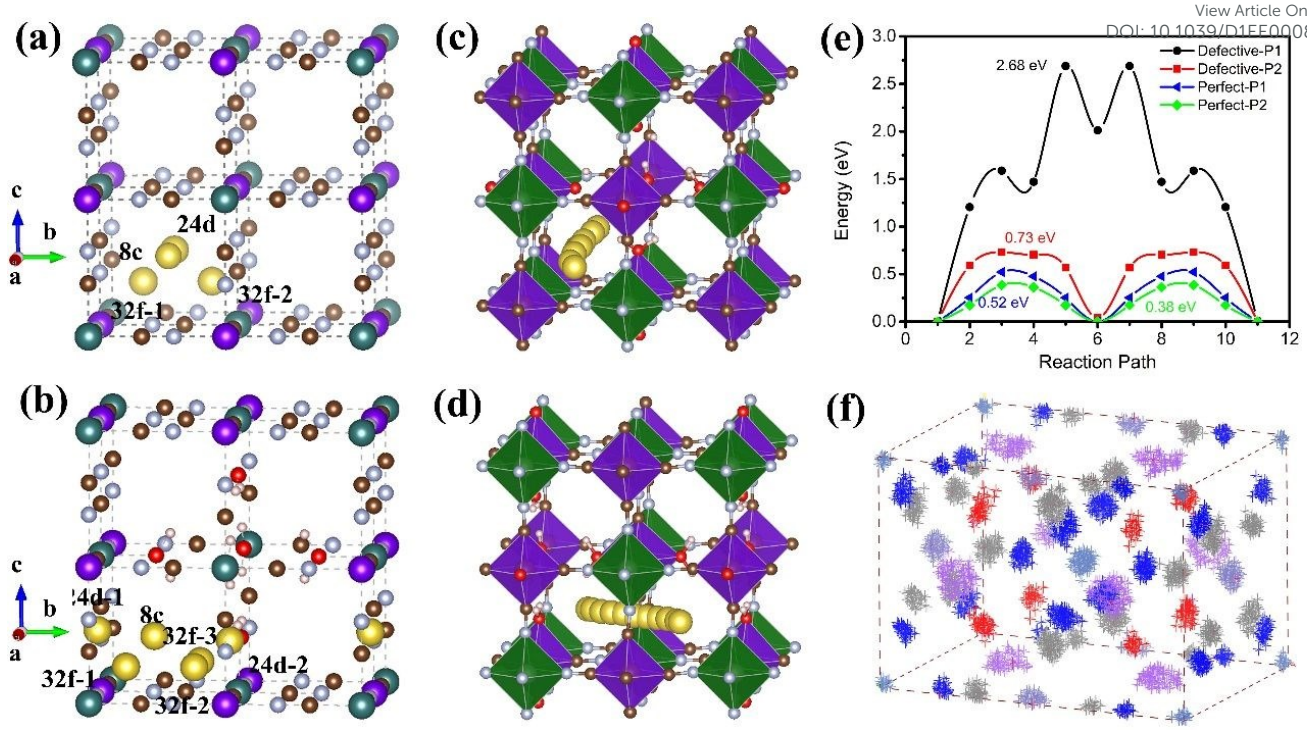

Fig. 4 | DFT calculation and thermomechanical analysis. a, Theoretical perfect crystal structure of Ni-based Prussian blue analogs with four possible interstices: 8*c* (body-centered), 24*d* (face-centered), 32*f*-1, and 32*f*-2 (32*f*-1 displaced from 8*c* positions toward N-coordinated corner; 32*f*-2 displaced from 8*c* positions toward C-coordinated corner). **b,** Defect crystal structure of Ni-based Prussian blue analogs with two additional interstices in the face-center and N/C-coordinated corner. **c, d,** Side views of two possible Na^+ migration paths in perfect and defect crystal structure, respectively. **e,** Corresponding migration energy of the two paths in different crystal structures. **f,** Thermal polarization analysis of atoms in the structure of SC-NiHCF.

framework. The sodiation potential in the 24*d* site around the defects is only about 1.01 V. Therefore, the defects in the Ni-Fe PBA framework are unfavorable for its use as a cathode.

The effect of defects on Na-ion diffusion was also investigated. Two Na-ion diffusion pathways are considered (Fig. 4): (1) Na ions pass through the defect-center along an axis (Fig. 4c); (2) Na ions transfer along an S-shaped pathway that bypasses the nearest defect center (Fig. 4d). The corresponding Na-ion diffusion behavior in the perfect PBA framework was also studied. As shown in Fig. 4e, Na ion that diffusing through the S-shaped pathway shows a lower energy barrier in both frameworks, which indicates that the S-shaped route is preferable for Na-ion diffusion. Moreover, the Na-ion diffusion around the defect center energy barrier is much higher than that of perfect PBA. The large energy difference (2.68 eV) across the defect-center leads to sluggish Na-ion migration. Thus, the decrease in defect density in the PBA framework is favorable for Na-ion migration resulting in the much-enhanced rate performance of SIB.

SC-NiHCF achieves an excellent rate performance via a solid solution mechanism. Fig. 4e and d show a "snapshot" of SC-NiHCF in time of the structure where the distortion of the polyhedral framework structures is obvious.[26, 58, 59] The models produced by using total scattering data represent the structure at an instant of time, and any ions undergoing motion appear "frozen"[60]. Information regarding the static and dynamic disorder could be extracted from the refinement of RMC configuration into a single unit cell. Fig. 4f shows the distribution cloud of all atoms in NiHCF. The results indicate that the displacement of sodium is huge along the c-axis. Although the structure of NiHCF has been studied in detail,[49, 61, 62] the structural relationships among the different components are not well understood due to experimental limitations.

The current-voltage curves under different rates (0.1–20 C) indicate that SC-NiHCF undergoes a solid-solution transformation mechanism. The solid-solution mechanism is more dynamically favorable than the typical two-phase mechanism, which is kinetically limited due to two-phase nucleation. Growth and ion diffusivity are limited when the ion goes through a moving phase boundary.

The aforementioned PDF data and RMC simulation suggest that frustrated sodium ions are disordered. displaying liquid-like sublattice. The role of frustration[63] could flatten the energy landscape, preventing locking of ions in deep energy minima, resulting in local split-site and rapid phase-transformation behavior[64]. Thus, the disordered sodium ions will lose their long-range correlation when far from equilibrium conditions[65]. They could then randomly and rapidly exchange their sites, resulting in an excellent rate performance. To investigate the relationship of sodium and water, we performed local correlation coefficient calculations. Local correlation coefficients (LCCs) represent the probability of finding an atom within a specific crystallographic shell. This allows the detection of solute arrangements in complex solid solutions. The solute atom pairs are more likely to be local neighbors at higher values, thus, larger solute clusters can occur with increased

Published on 22 March 2021. Downloaded on 3/25/2021 5:13:29 AM.

Energy & Environmental Science Accepted Manuscript

Please do not adjust margins

Table 2 | The generalized multicomponent short-range order parameter calculation.

View Article Online
DOI: 10.1039/D1EE00087J

Bond	Neutron model	X-ray model
O-O	0.2239	0.3104
O-Na	0.2740	0.2609
Na-Na	0.3758	0.3014
Na-O	0.126	0.127

probabilities.[66] Local correlation coefficients (LCC) were calculated (Table 2). The calculation details are in the supporting information. The calculation results show that the LCC parameter of Na-Na pairs equals 0.3758. This is larger than that of any other atomic pairs and suggests that sodium ions are most likely together. However, the LCC parameter of the Na-O atomic pair is 0.126.

As mentioned above, there are more neighboring atom pairs at higher values. This result indicates that within the specific shell, the oxygen seems to be close to sodium while sodium tends to be away from oxygen. Thus, most sodium atoms are distributed individually, while a small number of sodium ions are surrounded by a large amount of H_2O molecules. Whether the disorder and frustration originating from complex interaction of Na and water or host distortion needs deeper understanding and is beyond the scope of this study. Our results indicate local symmetry lowering could prevent Na from settling into low-entropy arrangement and resulting Na sublattice frustration, which may be a promising recipe for the designing of high-rate cathode materials.

According to the *in-situ* XRD and DFT calculations, the high reversibility and fast migration rate of sodium-ion shortage performance can be attributed to the following reasons: (1) the excellent cycling stability (0.1675% capacity fading per 100 cycles) is due to the "quasi-zero-strain" characteristics of SC-NiHCF that undergoes a negligible lattice distortion from 10.315 to 10.039 Å (~2.68% volume change) during the full Na^+ insertion/extraction process. Consequently, the negligible structural distortion could prevent the fracture of the PBA framework and ensure a superior cycling life. (2) The PBAs prepared via self-healing significantly reduce the content of $[Fe(CN)_6]^{3-/4-}$ vacancies and water molecules, which makes the frameworks of PBAs vulnerable and fragile, leading to the collapse of the water molecules and organic electrolytes during the side reaction. This consequently enhances their cycling performance. (3) The DFT and thermal analysis results indicate

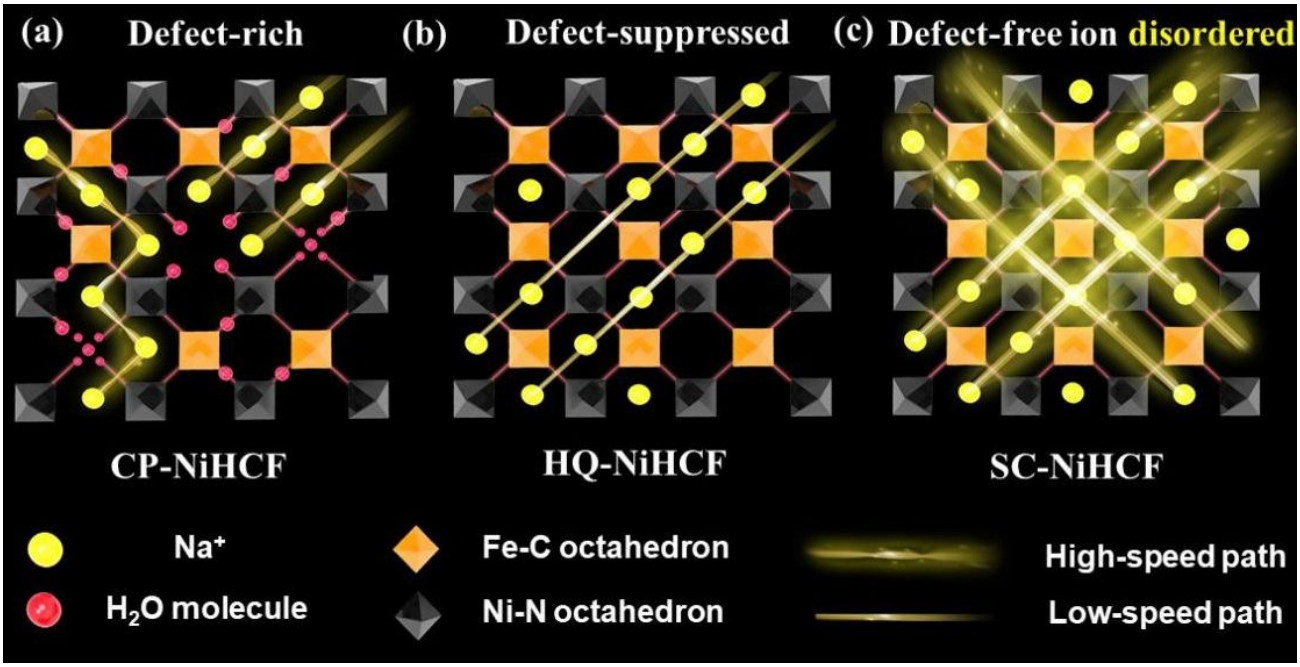

Fig. 5 | Na^+ migration paths for three kinds of PBAs. a, A schematic of Na^+ migration paths in defect-rich CP-NiHCF blocked by H_2O molecules and defects. **b**, Schematic of low-speed Na^+ migration paths in defect-suppressed HQ-NiHCF. **c**, Schematic of high-speed Na^+ migration paths in defect-free Na^+ disordered SC-NiHCF.

This journal is © The Royal Society of Chemistry 20xx

Please do not adjust margins

Published on 22 March 2021. Downloaded on 3/25/2021 5:13:29 AM.

Energy & Environmental Science Accepted Manuscript

View Article Online
DOI: 10.1039/D1EE00087J

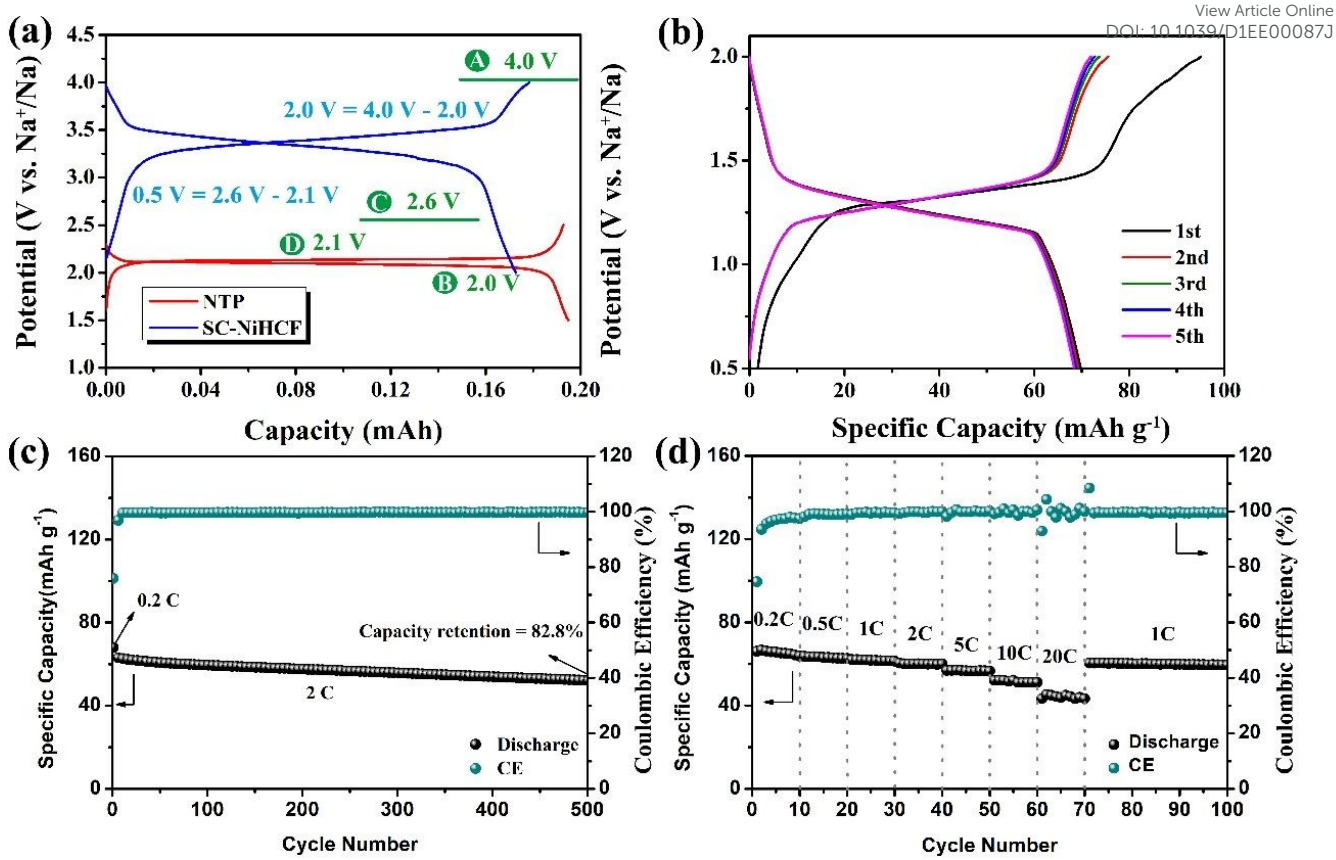

Fig. 6 | The electrochemical performance of SC-NiHCF/NTP full-cell. a, Half-cell charge and discharge voltage profiles of SC-NiHCF and NTP at a current density of 0.1 C (1 C = 80 mA g^{-1}). **b**, Full-cell charge and discharge curves at a current density of 0.1 C. **c**, Long-term cycling performance at a current density of 2 C. **d**, Rate performance of the full-cell at a current density range of 0.2–20 C (specific capacity calculated by the cathode mass).

that the migration energy of Na ions in a water-rich structure is higher than that in the water-suppressed framework because the rapid movement of Na ions is hindered by the water molecules in the lattice of SC-NiHCF. Therefore, fast Na ion migration could be realized by reducing the number of water molecules by tuning the synthesis and possible Na^+ ion migration mechanism in three kinds of PBAs are displayed in Fig. 5, in which the unhindered 3D Na-ion fast diffusion occurs in the defect-free and disordered frameworks of SC-NiHCF (Fig. 5c).

Full cell performance

Fig. 6a exhibits the charge/discharge curves matchup of SC-NiHCF and $NaTi_2(PO_4)_3$ (NTP) (10% excess) full cells. Fig. 6b shows that the initial charge and discharge capacity of the SC-NiHCF cathode at a current density of 8.5 mA g^{-1} were 95.1 and 69.8 mAh g^{-1}, respectively, corresponding to the initial CE of 73.4%. This value is attributed to irreversible reactions and the formation of Na^+-permeable solid electrolyte interface (SEI) layers on both electrodes[43]. The rate capability of the SC-NiHCF/NTP full cell is shown in Fig. 6d and supplementary Fig. 25. Note that the specific capacity remains nearly 44 mAh g^{-1} at the current density of 1700 mA g^{-1}, which corresponds to 67% of the reversible capacity at the rate of 17 mA g^{-1}. Fig. 6c shows that the full cell delivers 82.8% of the initial capacity over 500 cycles at the current density of 170 mA g^{-1}. This brilliant rate and cycle performance are superior to any reported PBA-base full-cell suggesting the enormous potential of SC-NiHCF as SIB cathode for fast-charging grid-scale energy storage applications and higher energy density full cells could be obtained by pairing SC-NiHCF with other kinds of anode materials.

Conclusions

In summary, PBAs are model three-dimensional MOFs prepared via a novel self-healing synthesis method. They exhibit high specific capacity, excellent fast-charging ability, and long lifespan as cathode materials for SIBs. Multiple characterization experiments and DFT calculations demonstrate that the local structure and guest cation behavior on the atomic scale are highly susceptible to the crystal ambient environment and content of water molecules. These are critical to open topologies and provoke Na^+ migration barriers. The as-prepared defect-free PBAs electrode materials have cation disorder sites and large host sites and can effectively avoid volume distortion during the insertion/extraction processes. Thus, they exhibit fast-ionic conduction ability for sodium-ion intercalation and a prolonged cycle life via a quasi-zero-strain nonequilibrium two-phase transition mechanism. The facile synthesis, low-cost, and superior electrochemical performance of our PBAs make them competitive cathode materials for grid-scale energy storage applications.

Published on 22 March 2021. Downloaded on 3/25/2021 5:13:29 AM.
Energy & Environmental Science Accepted Manuscript

Author Contributions

J.P., M.O. and J.H. conceived the idea. M.O. and P.Z. performed the Pair Distribution Function characterization. J.P., H.Y., W.Z. and P.W. synthesized the materials and performed the electrochemical experiments. X.S. and S.G. performed the EXAFS experiments and analyzed the data. B.Z., L.M., and J.J. performed the DFT calculation. J.P., Y.D., and F.W. performed the in situ XRD measurements and J.P. analyzed the data. J.A.A., M.T.F.D. and C.A.L. collected the ND and synchrotron XRD patterns and analyzed the data together with M.O. J.P., Y.L., J.F. and Y.L. characterized the materials. M.O. and Y.L. performed the refinement. J.P. and J.H. wrote the manuscript with input from all co-authors.

Conflicts of interest

There are no conflicts to declare.

Acknowledgements

J. H. thanks the National Natural Science Foundation of China (Grant Nos. 51772117 and 51732005) and the National Key R&D Program of China (Grant Nos. 2016YFB010030X and 2016YFB0700600) for financial support. We thank the Analytical and Testing Centre and the State Key Laboratory of Materials Processing and Die & Mould Technology of HUST for the material characterization. J. A. A. acknowledges the financial support given by the Spanish Ministry of Economy and Competitiveness to the project MAT2017-84496-R. X. S. thanks the National Natural Science Foundation of China (Grant Nos. 11905081). We are grateful to ILL (Grenoble, France) for providing the neutron beam time.

Notes and references

1 M. Armand and J.-M. Tarascon, Nature, 2008, **451**, 652.
2 B. Dunn, H. Kamath and J.-M. Tarascon, Science, 2011, **334**, 928.
3 M. R. Palacín and A. de Guibert, Science, 2016, **351**, 1253292.
4 G. Liang, Z. Wu, C. Didier, W. Zhang, J. Cuan, B. Li, K. Y. Ko, P. Y. Hung, C. Z. Lu and Y. J. A. C. I. E. Chen, Angew Chem Int Ed Engl, 2020, **59**, 10594.
5 J. Sun, H. W. Lee, M. Pasta, H. Yuan, G. Zheng, Y. Sun, Y. Li and Y. Cui, Nat Nanotechnol, 2015, **10**, 980.
6 K. J. Griffith, K. M. Wiaderek, G. Cibin, L. E. Marbella and C. P. Grey, Nature, 2018, **559**, 556.
7 Z. Tu, S. Choudhury, M. J. Zachman, S. Wei, K. Zhang, L. F. Kourkoutis and L. A. Archer, Nature Energy, 2018, **3**, 310.
8 B. W. Zhang, T. Sheng, Y. D. Liu, Y. X. Wang, L. Zhang, W. H. Lai, L. Wang, J. Yang, Q. F. Gu, S. L. Chou, H. K. Liu and S. X. Dou, Nature communications, 2018, **9**, 4082.
9 M. C. Lin, M. Gong, B. Lu, Y. Wu, D. Y. Wang, M. Guan, M. Angell, C. Chen, J. Yang, B. J. Hwang and H. Dai, Nature, 2015, **520**, 325.
10 Y. Jin, K. Liu, J. Lang, D. Zhuo, Z. Huang, C.-a. Wang, H. Wu and Y. Cui, Nature Energy, 2018, **3**, 732.
11 X. Xu, D. Zhou, X. Qin, K. Lin, F. Kang, B. Li, D. Shanmukaraj, T. Rojo, M. Armand and G. Wang, Nature communications, 2018, **9**, 3870.
12 Y. Liang, Y. Jing, S. Gheytani, K. Y. Lee, P. Liu, A. Facchetti and Y. Yao, Nat Mater, 2017, **16**, 841.
13 B. Y. Ruan, H. P. Guo, Y. Y. Hou, Q. N. Liu, Y. F. Deng, G. H. Chen, S. L. Chou, H. K. Liu and J. Z. Wang, ACS Applied Materials & Interfaces, 2017, **9**, 37682.
14 H. Deng, C. J. Doonan, H. Furukawa, R. B. Ferreira, J. Towne, C. B. Knobler, B. Wang and O. M. J. S. Yaghi, 2010, **327**, 846.
15 H. Kim, H. Kim, Z. Ding, M. H. Lee, K. Lim, G. Yoon and K. Kang, Advanced Energy Materials, 2016, **6**, 1600943.
16 Q. Wang, C. Zhao, Y. Lu, Y. Li, Y. Zheng, Y. Qi, X. Rong, L. Jiang, X. Qi, Y. Shao, D. Pan, B. Li, Y. S. Hu and L. Chen, Small, 2017, **13,** 1701835.
17 M. I. Jamesh and A. S. Prakash, Journal of Power Sources, 2018, **378**, 268.
18 P. Yu, F. Wang, T. A. Shifa, X. Zhan, X. Lou, F. Xia and J. He, Nano Energy, 2019, **58**, 244.
19 H. Pan, Y.-S. Hu and L. Chen, Energy & Environmental Science, 2013, **6**, 2338.
20 X. Xiang, K. Zhang and J. Chen, Advanced materials, 2015, **27**, 5343.
21 C. Fang, Y. Huang, W. Zhang, J. Han, Z. Deng, Y. Cao and H. Yang, Advanced Energy Materials, 2016, **6**, 1501727.
22 X. Wu, Y. Qi, J. J. Hong, Z. Li, A. S. Hernandez and X. Ji, Angewandte Chemie, 2017, **56**, 13026.
23 R. Y. Wang, C. D. Wessells, R. A. Huggins and Y. Cui, Nano Lett, 2013, **13**, 5748.
24 K. Zhang, X. Han, Z. Hu, X. Zhang, Z. Tao and J. Chen, Chemical Society reviews, 2015, **44**, 699.
25 H. W. Lee, R. Y. Wang, M. Pasta, S. Woo Lee, N. Liu and Y. Cui, Nat Commun, 2014, **5**, 5280.
26 M. Pasta, C. D. Wessells, N. Liu, J. Nelson, M. T. McDowell, R. A. Huggins, M. F. Toney and Y. Cui, Nat Commun, 2014, **5**, 3007.
27 Y. You, X.-L. Wu, Y.-X. Yin and Y.-G. Guo, Energy & Environmental Science, 2014, **7**, 1643.
28 M. Pasta, R. Y. Wang, R. Ruffo, R. Qiao, H.-W. Lee, B. Shyam, M. Guo, Y. Wang, L. A. Wray, W. Yang, M. F. Toney and Y. Cui, J. Mater. Chem. A, 2016, **4**, 4211.
29 A. Zhou, W. Cheng, W. Wang, Q. Zhao, J. Xie, W. Zhang, H. Gao, L. Xue and J. Li, Advanced Energy Materials, 2020, 11, 2000943.
30 Q. Liu, Z. Hu, M. Chen, C. Zou, H. Jin, S. Wang, S. L. Chou, Y. Liu and S. X. J. A. F. M. Dou, 2020, **30**, 1909530.
31 J. Yin, Y. Shen, C. Li, C. Fan, S. Sun, Y. Liu, J. Peng, L. Qing and J. Han, ChemSusChem, 2019, **12**, 4786.
32 L. Wang, J. Song, R. Qiao, L. A. Wray, M. A. Hossain, Y. D. Chuang, W. Yang, Y. Lu, D. Evans, J. J. Lee, S. Vail, X. Zhao, M. Nishijima, S. Kakimoto and J. B. Goodenough, J Am Chem Soc, 2015, **137**, 2548.
33 J. Qian, C. Wu, Y. Cao, Z. Ma, Y. Huang, X. Ai and H. Yang, Advanced Energy Materials, 2018, **8**, 1702619.
34 X. Wu, M. Shao, C. Wu, J. Qian, Y. Cao, X. Ai and H. Yang, ACS Appl Mater Interfaces, 2016, **8**, 23706.
35 X. Wu, C. Wu, C. Wei, L. Hu, J. Qian, Y. Cao, X. Ai, J. Wang and H. Yang, ACS Appl Mater Interfaces, 2016, **8**, 5393.
36 C. Li, R. Zang, P. Li, Z. Man, S. Wang, X. Li, Y. Wu, S. Liu and G. Wang, Chem Asian J, 2018, **13**, 342.
37 J. Song, L. Wang, Y. Lu, J. Liu, B. Guo, P. Xiao, J. J. Lee, X. Q. Yang, G. Henkelman and J. B. Goodenough, J Am Chem Soc, 2015, **137**, 2658.
38 X. Yan, Y. Yang, E. Liu, L. Sun, H. Wang, X.-Z. Liao, Y. He and Z.-F. Ma, Electrochimica Acta, 2017, **225**, 235.
39 D. Su, A. McDonagh, S. Z. Qiao and G. Wang, Adv Mater, 2017, **29**, 1604007.
40 M. L. Aubrey, B. M. Wiers, S. C. Andrews, T. Sakurai, S. E. Reyes-Lillo, S. M. Hamed, C. J. Yu, L. E. Darago, J. A. Mason, J. O. Baeg, F.

View Article Online DOI: 10.1039/D1EE00388K

Published on 22 March 2021. Downloaded on 3/25/2021 5:13:29 AM.

Energy & Environmental Science Accepted Manuscript

This journal is © The Royal Society of Chemistry 20xx

Please do not adjust margins

View Article Online
DOI: 10.1039/D1EE00087J

Grandjean, G. J. Long, S. Seki, J. B. Neaton, P. Yang and J. R. Long, Nat Mater, 2018, **17**, 625.
41 Y. Xu, J. Wan, L. Huang, M. Ou, C. Fan, P. Wei, J. Peng, Y. Liu, Y. Qiu and X. Sun, Advanced Energy Materials, 2019, **9**, 1803158.
42 Y. Li, Z. Gao, F. Hu, X. Lin, Y. Wei, J. Peng, J. Yang, Z. Li, Y. Huang and H. Ding, Small Methods, 2020, **4**, 2000111.
43 J. Peng, J. S. Wang, H. C. Yi, W. J. Hu, Y. H. Yu, J. W. Yin, Y. Shen, Y. Liu, J. H. Luo, Y. Xu, P. Wei, Y. Y. Li, Y. Jin, Y. Ding, L. Miao, J. J. Jiang, J. T. Han and Y. H. Huang, Advanced Energy Materials, 2018, **8**, 1702856.
44 X.-H. Ma, Y.-Y. Wei, Y.-D. Wu, J. Wang, W. Jia, J.-H. Zhou, Z.-F. Zi and J.-M. Dai, Electrochimica Acta, 2019, **297,** 392.
45 L. Xue, Y. Li, H. Gao, W. Zhou, X. Lu, W. Kaveevivitchai, A. Manthiram and J. B. Goodenough, J Am Chem Soc, 2017, **139**, 2164.
46 D. Su, M. Cortie, H. Fan and G. Wang, Advanced materials, 2017, **29**, 1700587.
47 S. Hoshino, T. Sakuma, H. Fujishita and K. Shibata, J. Phys. Soc. Jpn, 1983, **52**, 1261.
48 Y. Huang, M. Xie, J. Zhang, Z. Wang, Y. Jiang, G. Xiao, S. Li, L. Li, F. Wu and R. Chen, Nano Energy, 2017, **39**, 273.
49 W. Ren, M. Qin, Z. Zhu, M. Yan, Q. Li, L. Zhang, D. Liu and L. Mai, Nano Lett, 2017, **17**, 4713.
50 Z. Ji, B. Han, H. Liang, C. Zhou, Q. Gao, K. Xia and J. Wu, ACS Appl Mater Interfaces, 2016, **8**, 33619.
51 Y. You, X. Yu, Y. Yin, K.-W. Nam and Y.-G. Guo, Nano Research, 2014, **8**, 117.
52 Y. You, X.-L. Wu, Y.-X. Yin and Y.-G. Guo, Journal of Materials Chemistry A, 2013, **1**, 14061.
53 R. Rehman, J. Peng, H. Yi, Y. Shen, J. Yin, C. Li, C. Fang, Q. Li and J. Han, RSC Advances, 2020, **10**, 27033.
54 M. J. Piernas-Muñoz, E. Castillo-Martínez, J. L. Gómez-Cámer and T. Rojo, Electrochimica Acta, 2016, **200**, 123.
55 B. Xie, P. Zuo, L. Wang, J. Wang, H. Huo, M. He, J. Shu, H. Li, S. Lou and G. Yin, Nano Energy, 2019, **61**, 201.
56 Y. You, X.-L. Wu, Y.-X. Yin and Y.-G. Guo, Journal of Materials Chemistry A, 2013, **1**, 14061.
57 L. Chen, H. Shao, X. Zhou, G. Liu, J. Jiang and Z. Liu, Nat Commun, 2016, **7**, 11982.
58 A. Firouzi, R. Qiao, S. Motallebi, C. W. Valencia, H. S. Israel, M. Fujimoto, L. A. Wray, Y. D. Chuang, W. Yang and C. D. Wessells, Nat Commun, 2018, **9**, 861.
59 C. D. Wessells, R. A. Huggins and Y. Cui, Nat Commun, 2011, **2**, 550.
60 D. A. Keen, J. Phys. Condens. Matter, 2002, **14**, R819.
61 Y. Lu, L. Wang, J. Cheng and J. B. Goodenough, Chem Commun, 2012, **48**, 6544.
62 Z. Wang, Y. Liu, Z. Wu, G. Guan, D. Zhang, H. Zheng, S. Xu, S. Liu and X. Hao, Nanoscale, 2017, **9**, 823.
63 D. Di Stefano, A. Miglio, K. Robeyns, Y. Filinchuk, M. Lechartier, A. Senyshyn, H. Ishida, S. Spannenberger, D. Prutsch, S. Lunghammer, D. Rettenwander, M. Wilkening, B. Roling, Y. Kato and G. Hautier, Chem, 2019, **5**, 2450.
64 S. Wall, S. Yang, L. Vidas, M. Chollet, J. M. Glownia, M. Kozina, T. Katayama, T. Henighan, M. Jiang, T. Miller, D. A. Reis, L. A. Boatner, O. Delaire and M. Trigo, Science, 2018, **362**, 572.
65 J. Shamblin, M. Feygenson, J. Neuefeind, C. L. Tracy, F. Zhang, S. Finkeldei, D. Bosbach, H. Zhou, R. C. Ewing and M. Lang, Nature materials, 2016, **15**, 507.
66 A. V. Ceguerra, M. P. Moody, R. C. Powles, T. C. Petersen, R. K. W. Marceau and S. P. Ringer, Acta Crystallogr A, 2012, **68**, 547-560.

Published on 22 March 2021. Downloaded on 3/25/2021 5:13:29 AM.

Energy & Environmental Science Accepted Manuscript

Please do not adjust margins